Chemical Science

ROYAL SOCIETY OF CHEMISTRY

EDGE ARTICLE

View Article Online
View Journal | View Issue

Cite this: *Chem. Sci.*, 2025, **16**, 14995

All publication charges for this article have been paid for by the Royal Society of Chemistry

Chemical and mechanical modifications of flexible metal–organic frameworks for enhancing photocatalysis†

Yi-Fan Liu,‡[b] Huihui He,‡[a] Lei Gao,[b] Rong-Ran Liang,[c] Ji Li,[a] Jinyi Huang,[a] Ya Yin,[b] Yuxuan Meng,[a] Yuxiu Zhong,[b] Rengan Luo,[b] Liang-Liang Zhang,*[a] Hong-Cai Zhou *[c] and Shuai Yuan *[b]

Postsynthetic modification (PSM) has been widely employed to enhance the functionality of metal–organic frameworks (MOFs) for applications such as gas storage, light harvesting, and catalysis. However, the critical role of framework flexibility in enabling diverse modification pathways and influencing framework properties remains underexplored. In this work, we demonstrate that flexible MOFs offer unique advantages for PSM, using the flexible PCN-128 as a platform for both chemical and mechanical modifications to enhance photocatalytic CO_2 reduction activity. Mechanical force induces piezochromic behavior, while sequential postsynthetic annulation reactions extend the π-conjugation of aromatic ligands within PCN-128, both modulating the energy band positions and enhancing visible light absorption. Single-crystal-to-single-crystal transformations were realized throughout the PSM process, offering valuable insights into the transformation process and structure–property relationships. Furthermore, metallo-phthalocyanine-based ligands (M-TcPC, M = Fe, Co, Ni) were introduced as catalytic sites for CO_2 reduction *via* PSM strategies. By optimizing the ratio of photosensitizers to catalytic sites, the modified catalysts achieved a remarkable CO_2 reduction rate of 838 μmol g^{-1} h^{-1} under visible light irradiation. This study highlights the untapped potential of flexible MOFs in applying postsynthetic modification strategies to develop advanced photocatalysts for sustainable energy conversion.

Received 16th April 2025
Accepted 19th July 2025

DOI: 10.1039/d5sc02797g

rsc.li/chemical-science

Introduction

Photocatalysis utilizes solar energy to drive chemical reactions, offering a promising strategy for sustainable energy conversion.[1–5] While traditional inorganic or organic semiconductors such as C_3N_4,[6] TiO_2,[7] and perovskites[8] have been studied extensively as photocatalysts,[9–11] their photocatalytic performance is often constrained by limited surface area, slow mass transport, and insufficient structural tunability.[12–16] In contrast, metal–organic frameworks (MOFs), composed of inorganic nodes and organic linkers, offer high surface areas, tunable pore environments, and modular architectures,[17–19] making them highly attractive platforms for photocatalysis.[20–24]

A key advantage of MOFs in the design of photocatalysts lies in their amenability to postsynthetic modification (PSM), which enables further enhancement in photoactivity beyond what can be achieved through conventional one-pot synthesis.[25–27] Through PSM, photoactive functionalities can be introduced or fine-tuned while maintaining the porosity and framework integrality of MOFs.[28–31] For example, Lin group designed a MOF incorporating cuprous photosensitizers with Re catalysts for photocatalytic CO_2 reduction to CO, achieving enhanced CO_2 reduction activity under visible light.[32] Meanwhile, various catalytic sites can be anchored into photoactive MOFs, and their ratios can be further optimized to achieve superior CO_2 reduction activity.[33] These examples demonstrate that PSM allows the precise placement of photosensitizers and catalytic sites, thereby unlocking new opportunities for photocatalysis in previously inert MOFs.

Despite the progress achieved through chemical PSM, the mechanical modification of MOFs remains largely unexplored. Flexible MOFs, which can undergo structural changes in response to external stimuli, present new opportunities for mechanical and chemical tuning. Mechanical forces can alter

[a]*Institute of Flexible Electronics (SIFE, Future Technologies), Strait Laboratory of Flexible Electronics (SLoFE), Fujian Normal University, Fuzhou, 350117, P. R. China. E-mail: ifellzhang@fjnu.edu.cn*

[b]*State Key Laboratory of Coordination Chemistry, School of Chemistry and Chemical Engineering, Nanjing University, Nanjing 210023, P. R. China. E-mail: syuan@nju.edu.cn*

[c]*Department of Chemistry, Texas A&M University, College Station, Texas 77843-3255, USA. E-mail: zhou@chem.tamu.edu*

† Electronic supplementary information (ESI) available. CCDC 2395420, 2373983–2373985. For ESI and crystallographic data in CIF or other electronic format see DOI: https://doi.org/10.1039/d5sc02797g

‡ These authors contributed equally to this work.

the structure or conformation of MOFs, leading to changes in their electronic properties. A well-known example is piezochromic MOFs, which exhibit fluorescence changes under mechanical stress, making them suitable for applications such as mechanical sensing and security paper.[34] In addition to mechanical tuning, flexibility in MOFs also enhances the scope of chemical modifications as many modification reactions require the unit cell adjustments or bond rearrangements, which are not feasible in rigid frameworks. For example, Zhou, Su, Liu, and others have demonstrated postsynthetic linker installation in flexible Zr-MOFs, incorporating linkers of varying lengths to generate diverse structures with enhanced gas storage and catalytic performance.[35–38] However, few studies simultaneously explore the effects of mechanical forces and chemical modifications on the band gap structure and photocatalytic performance to our knowledge.

In this study, we selected the flexible MOF, PCN-128, and systematically tuned its properties through both mechanical and chemical modifications. Mechanical forces induced piezochromic behavior, while sequential postsynthetic annulation reactions extended the π-conjugation of aromatic ligands, both contributing to band position adjustments and visible light absorption enhancement. Notably, single-crystal-to-single-crystal (SC-to-SC) transformations were realized throughout the PSM process, allowing the monitoring of the structural transformation process by single-crystal X-ray diffraction. We demonstrated that flexibility is essential for successful PSM, as rigid MOF analogues remained inert to mechanical forces and annulation reactions. Additionally, we incorporated metallophthalocyanine-based ligands (M-TcPC, M = Fe, Co, Ni) as catalytic CO_2 reduction sites through PSM, achieving a remarkable reduction rate of 838 μmol g^{-1} h^{-1} under visible light. Transient absorption spectroscopy revealed that efficient energy transfer from the π-conjugated aromatic linkers to Co-TcPC played a key role in enhancing catalytic activity. This study underscores the high tunability of flexible MOFs through combined mechanical and chemical modifications, paving the way for the rational design and fine-tuning of MOF-based photocatalysts.

Results and discussion

Chemical and mechanical modifications of flexible PCN-128

PCN-128 was selected as a matrix because of its structural flexibility, high chemical stability, and mesoporosity.[39] We use both mechanical and chemical modifications to engineer the band gap and incorporate CO_2 catalytic sites into PCN-128. PCN-128 is composed of eight-connected $Zr_6O_4(OH)_4$ clusters linked by four-connected rectangular ETTC (ethene-tetrayl-tetrakis(biphenyl-carboxylate)) linkers, forming a highly porous framework with **csq** topology (Fig. 1a and b). The unique **csq** topology and flexible ETTC linkers endow PCN-128 with high structural tunability. Previously, we observed the piezofluorochromic behavior of PCN-128, where mechanical pressure induced compression of the ETTC linker and contraction along the *c*-axis of the PCN-128 lattice.[39] This compression resulted in a color change from white to yellow, and the resulting phase is referred to PCN-128Y (Fig. 1e and f). We further explored the chemical modification of PCN-128 *via* Scholl reactions to transform the ETTC linker into conjugated aromatic linkers, enhancing visible light absorption. Treating PCN-128 in 4.9 mM and 72.1 mM $FeCl_3$ solutions for an hour transformed ETTC into DPTC (9,10-diarylphenanthrenes tetratopic carboxylate) and DBTC (dibenzo[*g*,*p*]chrysenes tetratopic carboxylate), respectively (Fig. 1b–d and Scheme S2†).[40,41] These partially and fully oxidized products were named PCN-129 and PCN-130, respectively. The successful transformations were confirmed by ^{1}H NMR spectra of digested samples, where the disappearance of the original peaks at 7.18 ppm and the emergence of new peaks at 9.50 ppm for PCN-129 and 9.25 ppm for PCN-130 corresponded to the formation of the DPTC and DBTC linkers (Fig. S2–S4†). In PCN-128, 128Y, 129, and 130, each Zr_6 cluster is connected to 8 carboxylate linkers, leaving four uncoordinated Zr sites for post-synthetic installation of secondary linkers. Therefore, M-TcPC was anchored into PCN-128, 128Y, 129, and 130 through solvent-assisted ligand incorporation (Fig. 1k–m).

PSM process monitored *via* single-crystal X-ray diffraction

Previously, PCN-128 has only been synthesized as crystalline powders. By carefully controlling the reaction conditions, we successfully obtained single crystals of PCN-128, allowing for direct characterization of structural transformation *via* single crystal X-ray diffraction (SCXRD). Single crystal structures of PCN-128, PCN-128Y, PCN-129, and PCN-130 all crystallize in the hexagonal *P*6/*mmm* space group. Their frameworks consist of $Zr_6O_4(OH)_4$ clusters linked by rectangular linkers, sharing a similar framework structure with **csq** topology. The mechanical squeeze of ETTC and sequential transformation of ETTC into DPTC and DBTC were clearly observed (Fig. 1f–j). In PCN-128, the tetraphenylethylene moieties have four phenyl rings rotated approximately 51° out of the plane due to the steric hindrance of hydrogen atoms from adjacent phenyl rings. Under pressure-induced stimulus, the rotation angle increases to 70° in PCN-128Y. Upon transformation to PCN-129, two of these phenyl rings and the ethylene group merge into a planar phenanthrene moiety, while the remaining two phenyl rings rotate approximately 5 degrees off the plane. In PCN-130, all four phenyl rings and the ethylene group merge into a fully conjugated dibenzo[*g*,*p*]chrysene structure, which is nearly coplanar (Fig. S5–S8†).

Interestingly, the mechanical modification and post-synthetic annulation reactions are accompanied by changes in unit cell dimensions. The *c*-axis length shrinks from 16.64 Å in PCN-128 to 15.13 Å in PCN-128Y, 15.68 Å in PCN-129, and further to 15.17 Å in PCN-130. Conversely, the *a*-axis length expands from 49.04 Å in PCN-128 to 50.71 Å in PCN-128Y, 50.27 Å in PCN-129, and 50.08 Å in PCN-130. This unit cell change is attributed to the conformational alteration of the linker during the annulation reactions, which covalently connects adjacent phenyl rings along the *c*-axis. It is important to note that the framework flexibility of PCN-128 is crucial for the success of postsynthetic annulation reactions. To assess the role of

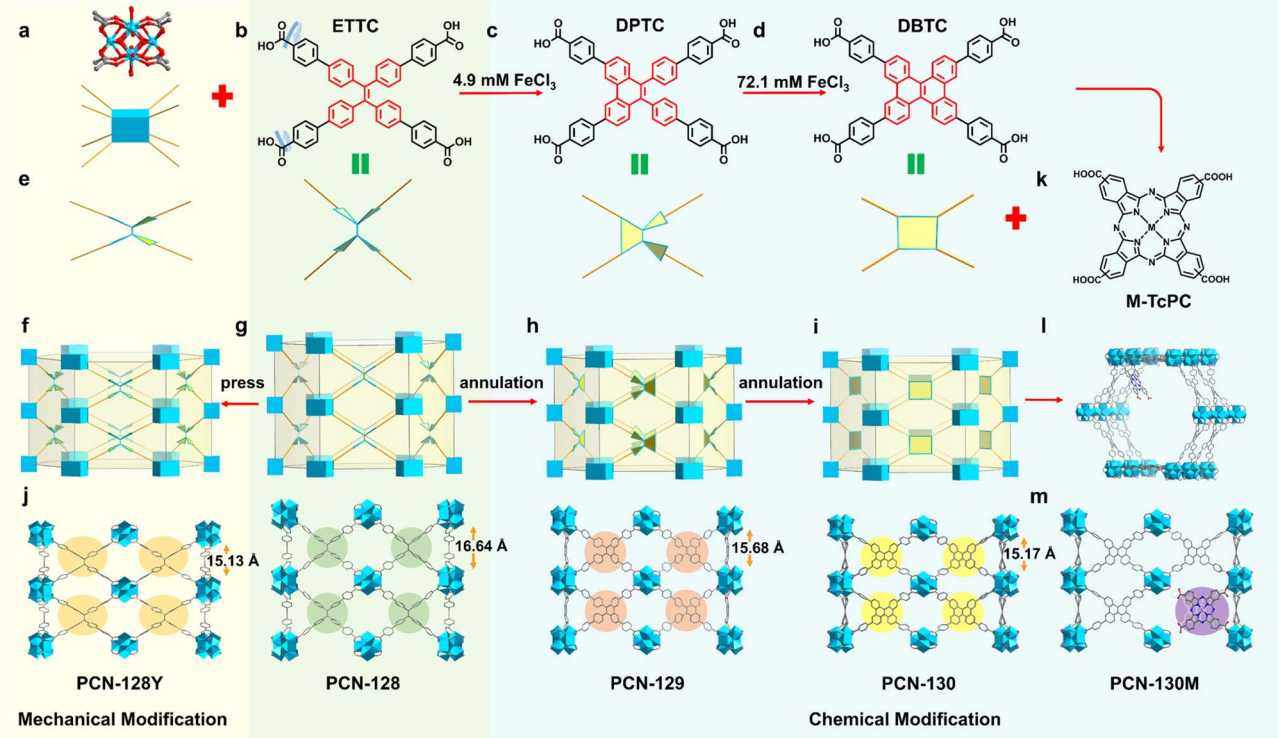

Fig. 1 (a) Zr_6 cluster and the corresponding schematic diagram. (b) The ETTC linker. (c) DPTC and (d) DBTC from sequential annulation of ETTC and the corresponding schematic diagrams. (e) Schematic diagram of pressed ETTC linker. Schematic diagram of (f) PCN-128Y, (g) PCN-128, (h) PCN-129 and (i) PCN-130. (j) Single-crystal structures of all synthesized samples viewed along the *b* direction. Linkers were highlighted for distinction. (k) The extra activate site M-TcPC. Schematic presentation of PCN-130M structure viewed along the (l) *b* and (m) *c* direction. Color scheme: Zr, sky blue; C, gray; N, blue; O, red; M, purple spheres. H atoms are omitted for clarity.

flexibility in chemical modification, we used a rigid framework PCN-94 as a control group.[42] PCN-94 contains 12-connected Zr_6 clusters and ETTC ligands but exhibits a rigid framework with a 4,12-connected **ftw** topology. Although both PCN-94 and PCN-128 are based on Zr_6 clusters and ETTC ligands, their differing connectivities and topologies lead to different levels of flexibility. Unlike PCN-128, the rigid PCN-94 could not undergo the annulation reaction under parallel experimental conditions, as confirmed by ^{1}H NMR spectra (Fig. S9 and S10†). Furthermore, mechanical compression did not induce any structural change in PCN-94. These control experiments highlight that flexibility is essential for successful PSM through mechanical forces and chemical annulation reactions.

It should be noted that PCN-129 and PCN-130 can only be synthesized by PSM of PCN-128. The direct solvothermal synthesis of PCN-129 and PCN-130 using Zr(IV) precursors and corresponding DPTC and DBTC linkers failed to yield crystalline products. We propose that this is because the free conformations of DPTC and DBTC linkers do not match the requirements of PCN-129 and PCN-130 structures. In the framework structures of PCN-128, PCN-129, and PCN-130, the carboxylate groups are rotated approximately 85° from the plane of the square planar linkers. In contrast, the angles are approximately 36.6° for DPTC and 49.0° for DBTC in their free molecular forms (Fig. S11 and S12†). These results highlight the critical role of postsynthetic annulation in achieving MOFs with conjugated aromatic linkers.

Structural characterization and stability evaluation

Powder X-ray diffraction (PXRD) was collected to verify the phase purity of PCN-128, PCN-128Y, PCN-129, PCN-130, and PCN-130M (Fig. 2a and S13†). The peak position of the (100) lattice plane shifts forward accompanied by the annulation of PCN-128 to PCN-129 and is maintained during further oxidation to PCN-130, matching well with the simulations based on single crystal structures. Moreover, the PXRD patterns of PCN-130M are similar to those of PCN-130, indicating that the anchoring of Co-TcPC ligands did not affect the overall framework structure.

The permanent porosities of PCN-128, PCN-128Y, PCN-129, PCN-130, and PCN-130M were measured by N_2 adsorption–desorption at 77 K. All samples exhibit a typical type IV isotherm with a steep increase at $P/P_0 = 0.4$, indicative of mesoporous structures. Pore size distribution, calculated by NLDFT methods based on N_2 adsorption data, shows hierarchically porous structures with two types of pores which can be assigned to triangular micro-channels and hexagonal meso-channels in the crystal structure. Both mechanical compression and post-synthetic annulation reactions slightly reduced the N_2 total uptake and Brunauer–Emmett–Teller (BET) surface area of PCN-128, which aligns with the observed reduction in unit cell volume after these modifications (Fig. 2b, Table S1 and S2†). Anchoring Co-TcPC ligands into PCN-130 resulted in

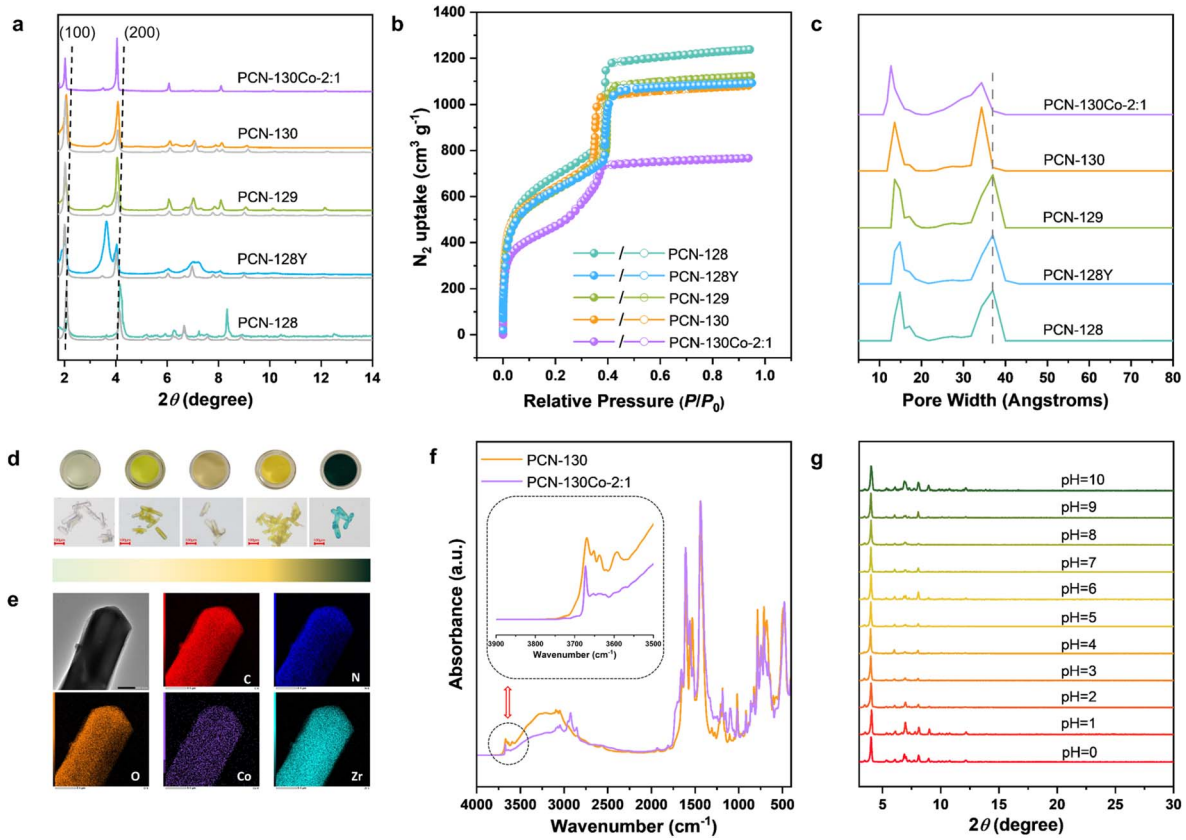

Fig. 2 (a) Simulated and PXRD patterns and (b) N_2 adsorption isotherms at 77 K of PCN-128, PCN-128Y, PCN-129, PCN-130, and PCN–130Co-2:1. (c) Pore size distribution of synthesized samples derived from N_2 adsorption isotherms. (d) Pictures and microscope images of PCN-128, PCN-128Y, PCN-129, PCN-130, and PCN-130Co-2:1. (e) TEM image of PCN–130Co-2:1 and corresponding element mapping. (f) The DRIFTS spectra of PCN-130 and PCN-130Co-2:1. Inset: the intensity decay of Zr–OH in the region from 3900 to 3500 cm^{-1}. (g) Stability test of PCN-130Co-2:1 in aqueous solution of pH 0–10 for 12 h.

a noticeable decrease in mesopore volume (Fig. 2c), indicating that the Co-TcPC primarily occupies the hexagonal mesochannels.

The sequential annulation process and subsequent Co-TcPC modification were visually observable through crystal color changes, from white to yellow and then to blue (Fig. 2d). The uniform color indicates the homogeneous composition of these samples throughout the crystal particles. Scanning electron microscopy (SEM), transmission electron microscopy (TEM), and elemental mapping using energy-dispersive X-ray spectroscopy (EDS) confirmed the retention of the rod-like crystal morphology and uniform distribution of Co-TcPC within the MOF particles (Fig. 2e and S14†). Additionally, infrared spectroscopy (Fig. S15 and S16†) and thermogravimetric analyses further confirmed the successful incorporation of Co-TcPC. The M-TcPC-functionalized samples exhibit reduced weight loss below 300 °C and increased loss above 300 °C, consistent with the substitution of terminal –OH/H_2O ligands by M-TcPC linkers. The experimentally observed residual weights align well with the calculated values based on the proposed MOF compositions (Fig. S17†). The coordination mode of Co-TcPC to the Zr_6 cluster was studied by diffuse reflectance infrared Fourier transform spectroscopy (DRIFTS). The –OH stretch of the Zr–OH groups initially observed at 3674 cm^{-1}, showed an intensity decrease upon coordination with Co-TcPC. Additionally, a new shoulder peak appeared at 1663 cm^{-1} corresponding to uncoordinated –COOH in Co-TcPC (Fig. 2f). Therefore, we propose a coordination model for Co-TcPC (Fig. 1l) in which Co-TcPC coordinates with Zr sites through one or two carboxylate groups, while the remaining carboxylic acid groups remain uncoordinated. X-ray photoelectron spectroscopy (XPS) further indicates the Co^{2+} species in PCN-130Co-2:1 (Fig. S18†).

The stability of PCN-130Co-2:1 was systematically studied by immersion in pH 0–10 aqueous solution for 12 h. No leaching of Co-TcPC or DBTC linkers was observed in the supernatant, as monitored by UV-vis spectra (Fig. S19†). Unchanged PXRD spectra demonstrated the maintained crystallinity during the stability test (Fig. 2g). In addition, PCN-130Co-2:1 also demonstrates higher mechanical stability than PCN-128 as indicated by the unchanged PXRD patterns after solvent removal and mechanical compression (Fig. S20†).

Physicochemical properties

Physicochemical properties of photoelectrical experiments of PCN-128, PCN-128Y, PCN-129, PCN-130, and PCN-130M were systematically investigated by UV-vis, Mott–Schottky

measurement, and DFT calculations. The UV-vis diffuse reflectance spectrum of PCN-128 shows no absorption in the visible light region. Under pressure, piezochromic behavior was observed in PCN-128Y accompanied by the redshift of absorption into the visible region. As the π-conjugation system was gradually extended, PCN-129 exhibited a slight redshift in absorption, while PCN-130 showed a significant redshift and enhanced absorption at 410 nm. After modifying PCN-130 with M-TcPC, PCN-130M shows a new absorption in the range from 600 to 800 nm assigning to the Q-band transitions of phthalocyanine (Fig. 3a and S21). The band gap energy (E_g) was calculated by Tauc plots to be 2.90 eV for PCN-128, 2.59 eV for PCN-128Y, 2.60 eV for PCN-129, 2.55 eV for PCN-130, and 1.47 eV for PCN-130Co-2:1 (Fig. S22 and S23†). The narrower bandgap corresponds to enhanced visible light absorption. Mott–Schottky measurement was conducted at different frequencies to determine the flat band energy. The flat band potentials were acquired with the values of −1.33, −1.24, −1.13, −0.83, and −0.62 V *vs.* normal hydrogen electrode (NHE) for PCN-128, PCN-128Y, PCN-129, PCN-130, and PCN–130Co-2:1, respectively (Fig. S24 and S25†). All samples displayed the typical positive slope of n-type semiconductors, where the conduction band (LUMO) equals the flat band potential. Therefore, the energy band structures of the MOFs obtained by Tauc and Mott–Schottky plots were displayed in Fig. 3b and S26, and the trend matched well with the HOMO and LUMO energy levels of the respective linkers (Fig. S27†).

To further investigate the influence of sequential annulation on the electronic structure, the total density of states (TDOS) and partial density of states (PDOS) were calculated *via* density-functional theory (DFT).[43–45] Fig. 3c represents the projected density of states aligned to the vacuum level for PCN-128 and PCN-130. For both PCN-128 and PCN-130, the conduction band (CB) was primarily located on the $Zr_6O_4(OH)_4$ clusters and the organic linker, whereas the valence band (VB) resided predominantly on the organic linker. More specifically, the VBs of both PCN-128 and PCN-130 are mainly composed of C and N orbitals, whereas the CBs originate from C, O, and Zr contributions. After the annulation reaction, an upshift in the VB was observed, leading to a narrower bandgap in PCN-130, underscoring its strong potential for efficient solar energy harvesting. A similar trend was observed in the alignment of the highest

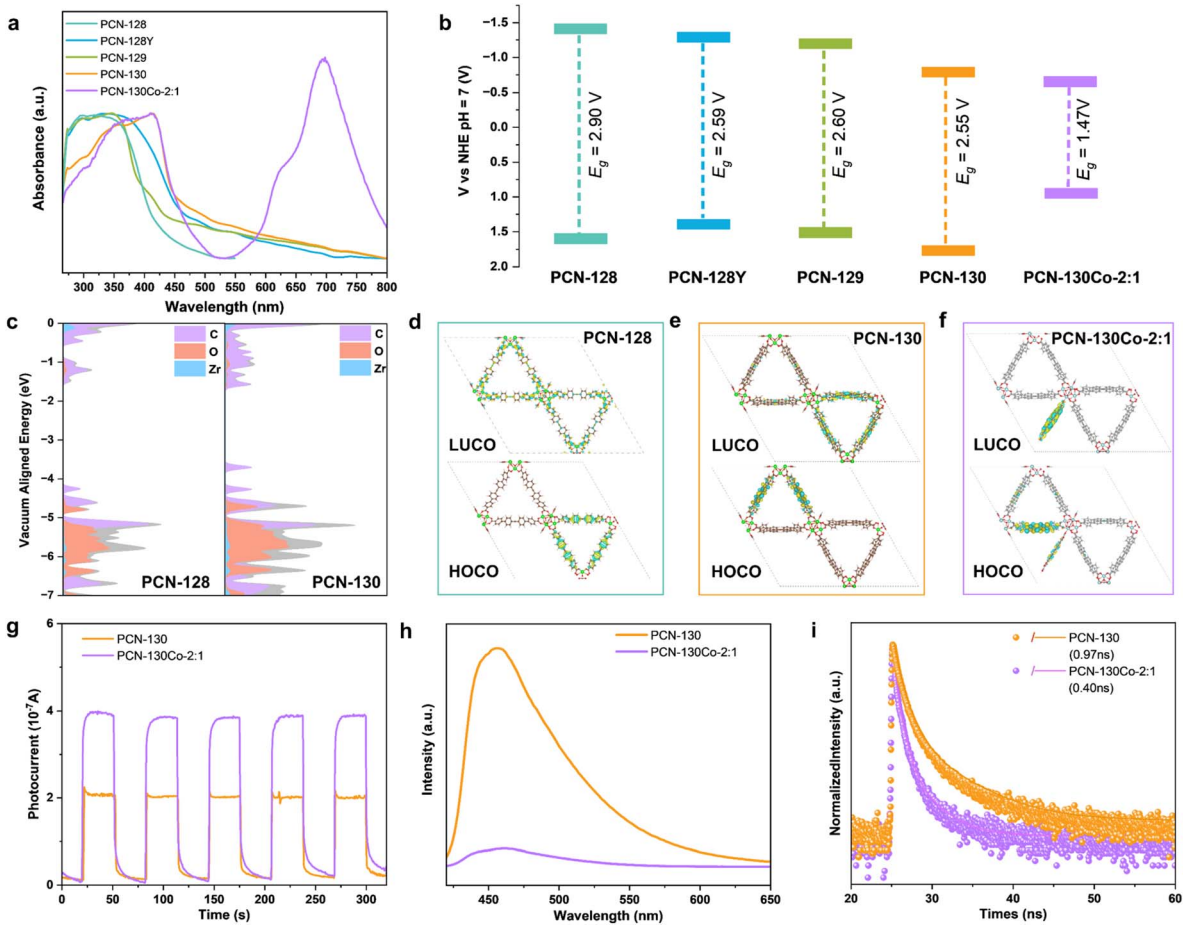

Fig. 3 (a) UV-vis spectra and (b) energy band gap value of PCN-128, PCN-128Y, PCN-129, PCN-130, PCN-130Co-2:1. (c) Calculated TDOS and PDOS of PCN-128 (left) and PCN-130 (right). HOCO and LUCO of (d) PCN-128, (e) PCN-130 and (f) PCN-130Co-2:1. (g) Transient photocurrent responses, (h) steady-state photoluminescence spectrum and (i) time-resolved photoluminescence decay plots of PCN-130 and PCN-130Co-2:1.

occupied crystal orbitals (HOCOs) and the lowest unoccupied crystal orbitals (LUCOs). The calculated bandgap between HOCO and LUCO decreased from 2.74 eV for PCN-128 to 2.10 eV for PCN-130 (Fig. 3c). Analysis of the charge density distribution of the respective HOCOs and LUCOs indicated that both MOFs exhibit spatially localized electronic states.[46] In contrast to PCN-130, PCN-130Co showed a redistribution of charge density, with the LUCO primarily localized on the Co-TcPC unit and HOCO primarily associated with the DBTC linker. Consequently, photoexcitation of PCN-130Co is expected to induce electron transfer from the photosensitizing DBTC linker to the Co-TcPC center (Fig. 3d–f).

Transient photocurrent response, photoluminescence spectra (PL), and time-resolved fluorescence decay spectroscopy were conducted to evaluate the photoelectron-hole separation efficiency (Fig. S28–S30†). After incorporating Co-TcPC, PCN-130Co-2:1 displays a higher photocurrent response intensity than PCN-130 under visible light irradiation, indicating more efficient photoinduced electron separation (Fig. 3g). The PL emission spectrum reveals weaker luminescence and time-resolved fluorescence decay spectroscopy shows a shorter fluorescence lifetime in PCN-130Co-2:1 suggesting effective energy/electron transfer from the DBTC fluorophore to the Co-TcPC center (Fig. 3h and i). These results demonstrate the enhanced charge separation and suppressed recombination facilitated by the incorporation of Co-TcPC.

Visible-light-driven CO_2 reduction

Encouraged by the well-defined ordered structure and promising photoelectric properties of PCN-130Co systems, we set out to investigate their photocatalytic CO_2 reduction performance. The photocatalytic reaction was conducted using 5 mg of catalyst in an acetonitrile/triethylamine (MeCN/TEA) mixed solution under visible light irradiation ($\lambda > 400$ nm) without additional photosensitizers or cocatalysts. The effect of photosensitizing linkers (ETTC, DPTC, and DBTC) on the photocatalytic activity was initially compared. PCN-130Co exhibited significantly higher CO_2 reduction activity compared to PCN-128Co, PCN-128YCo, and PCN-129Co, with CO as the main product. This enhanced performance can be attributed to the suitable energy band alignment and strong visible light absorption properties of the DBTC linkers. Additionally, the fully conjugated aromatic nature of DBTC likely contributes to the stabilization of the charge-separated state (Fig. 4a). Anchoring M-TcPC onto PCN-130 significantly enhanced the CO production rate, with Co-TcPC demonstrating the highest performance among the tested metals (Fig. 4b). Furthermore, the catalyst amount in each photocatalytic test was optimized to 5 mg, as lower loading resulted in reduced activity due to insufficient active sites, while excessive loading led to material waste (Fig. S31†). Lastly, the ratio between the photosensitizing DBTC linkers and catalytic Co-TcPC centers was optimized in PCN-130Co. PCN-130Co-2:1,

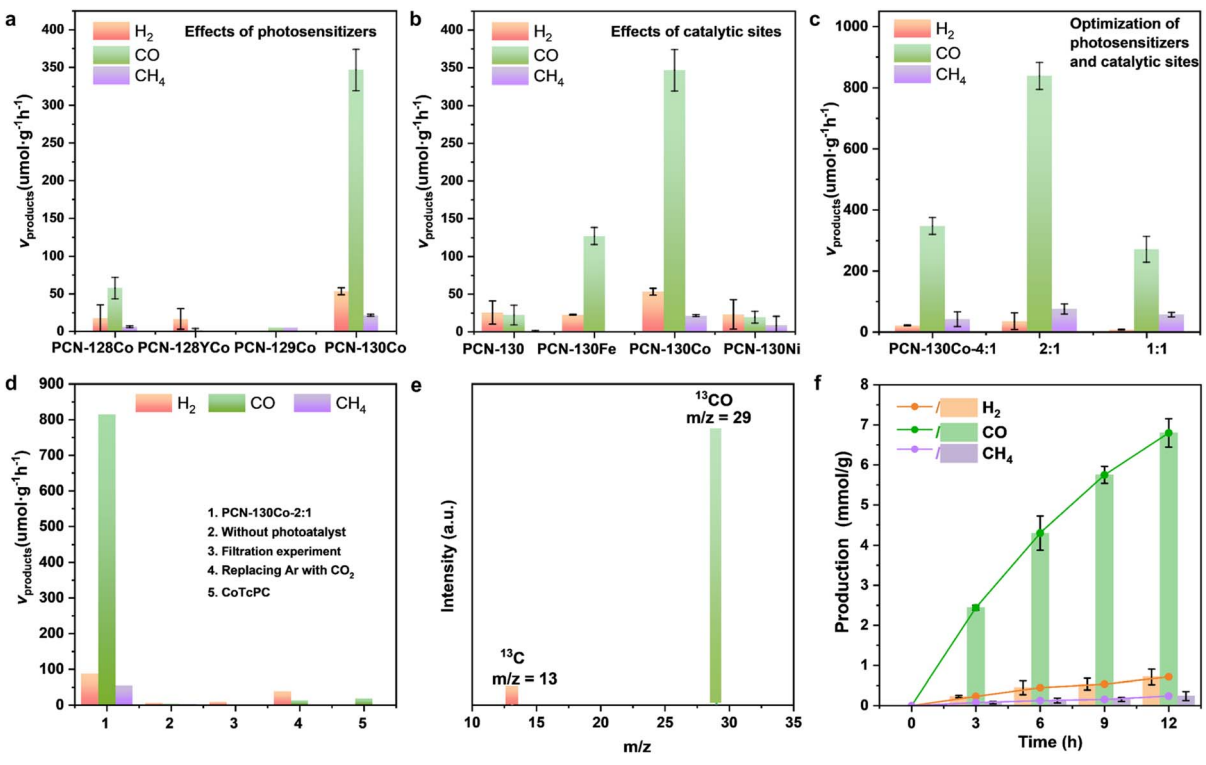

Fig. 4 (a) Effects of photosensitizers on photocatalytic CO_2 reduction in PCN–128Co, PCN-128YCo, PCN–129Co, and PCN-130Co. The ratio of Zr_6 cluster and M-TcPC is 4 : 1 without additional information. (b) Effects of different active sites and (c) optimization of photosensitizers and catalytic sites on photocatalytic CO_2 reduction. (d) The control experiments of CO_2 reduction performance over PCN-130Co-2:1 under altered conditions. (e) Mass spectra of ^{13}CO ($m/z = 29$) produced in the reduction of $^{13}CO_2$ over PCN-130Co-2:1. (f) Time-dependent CO_2 photoreduction performance of PCN-130Co-2:1.

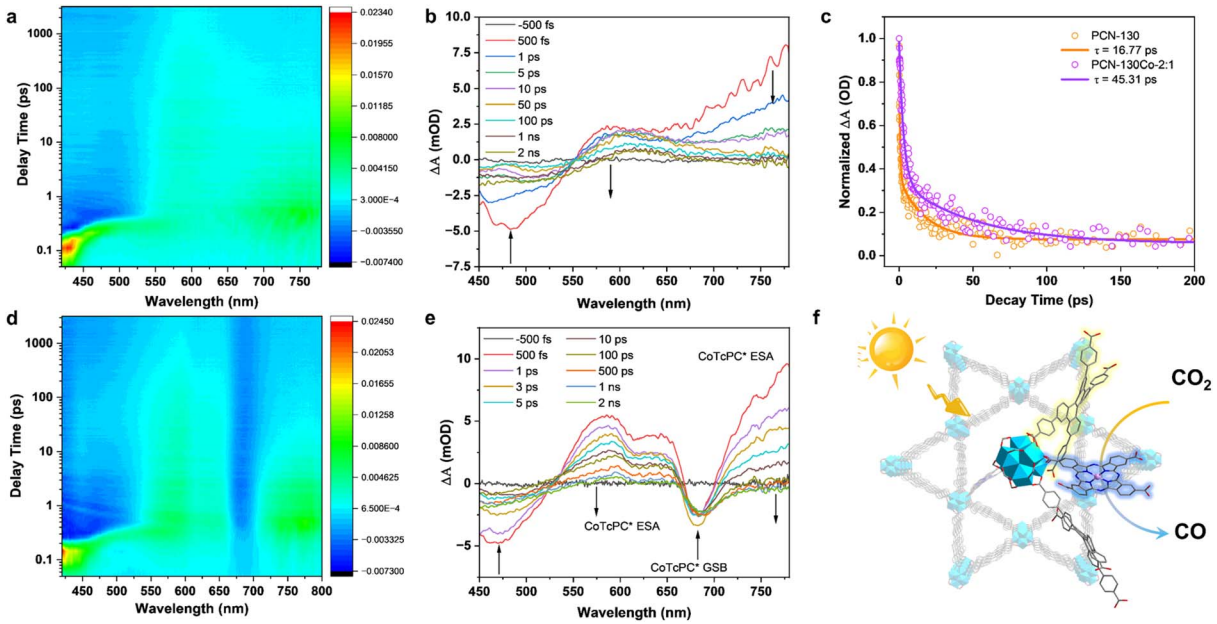

Fig. 5 Femtosecond TA contour maps of (a) PCN-130 and (d) PCN-130Co-2:1. The time-resolved TA spectra of (b) PCN-130 and (e) PCN-130Co-2:1 at different decay time. (c) Normalized kinetic profile probing at 775 nm. (f) Proposed mechanism diagram for energy transfer and photocatalytic CO_2 reduction of PCN-130Co-2:1.

with a DBTC to Co-TcPC ratio of 2 : 1, achieved the highest CO production rate of 838 μmol g^{-1} h^{-1} (Fig. 4c).

For comparison, control groups without the photocatalyst or without CO_2 showed no CO_2 reduction products. Additionally, molecular Co-TcPC exhibited low activity due to the absence of photosensitizing DBTC. Filtration experiments confirmed the heterogeneous nature of the catalytic reaction, as the filtrates displayed no activity (Fig. 4d). To further confirm the source of the CO product, the $^{13}CO_2$ isotopic labeling experiment was conducted. The detection of ^{13}CO peaks at $m/z = 29$ confirmed that the reduction products originated from $^{13}CO_2$, rather than the decomposition of catalysts or solution (Fig. 4e). Moreover, PCN-130Co-2:1 exhibited sustainable photocatalytic activity under visible light illumination for 12 h (Fig. 4f). The performance of PCN–130Co-2:1 remained consistent during three consecutive runs (Fig. S32†). PXRD test indicated the intact structure of PCN-130Co after photocatalytic CO_2 reduction, confirming its high stability (Fig. S33†).

The femtosecond transient absorption (fs-TA) spectroscopy measurement was performed to elucidate the excited state dynamics of PCN-130 and PCN-130Co-2:1. TA contour map and spectra at selective timepoints indicated that DBTC was photoexcited, producing the stimulated emission (SE) peak at 455 nm.[47,48] Simultaneously, charge transfer (CT) state and excited-state absorption contribute two new peaks around 580 nm and 780 nm (Fig. 5a and b). Compared with PCN-130, PCN-130Co-2:1 shows a negative peak at 680 nm, attributed to the ground-state bleaching (GSB) of Co-TcPC. The two new peaks at 575 nm and 775 nm correspond to the excited-state absorption (ESA) of Co-TcPC (Fig. 5d and e).[49] However, the CT peak and ESA of DBTC cannot be distinctly distinguishable because of the partial overlap with the EAS peaks of Co-TcPC. Notably, the SE of DBTC linkers and ESA peaks of Co-TcPC reached the maximum at 550 fs, while the GSB peak progressively increased until 3 ps and eventually dominated with longer time delays, suggesting the stable charge-separated state. Furthermore, the TA kinetics analysis and second-order function fitting at 775 nm reveal the average lifetime of 16.77 ps for PCN-130 and 45.31 ps for PCN-130Co-2:1, respectively. Thus, we propose that the energy transfer from DBTC to Co-TcPC increases the excited-state lifetime and suppresses electron–hole recombination under photoexcitation (Fig. 5c–f). The efficient energy transfer from the DBTC linker to the Co-TcPC catalytic center plays a crucial role in promoting visible-light-driven CO_2 reduction, making PCN-130Co a highly promising material for photocatalytic applications.

Conclusions

In conclusion, we systematically explored the PSM of the flexible MOF PCN-128 through both mechanical and chemical approaches to enhance photocatalytic performance. Sequential annulation of ETTC linkers transformed PCN-128 into PCN-130, effectively narrowing the bandgap and improving visible light absorption. Furthermore, introducing metallo-phthalocyanine-based ligands (M-TcPC, M = Fe, Co, Ni) into the framework provided additional catalytic sites, further boosting CO_2 reduction activity. The optimized catalyst, PCN-130Co-2:1, achieved an impressive CO_2 reduction rate under visible light by integrating photosensitizers and catalytic centers, enabling efficient energy transfer and prolonging the excited-state lifetime. This study emphasizes the critical role of framework flexibility in facilitating PSM by enabling structures that are inaccessible through conventional one-pot synthesis,

particularly for conformationally mismatched ligands. Our results further highlight the potential of mechanical and chemical modifications of flexible MOFs to optimize both the bandgap and active sites, thus enhancing photocatalytic efficiency. These new insights will inspire the rational design of advanced MOF-based photocatalysts for energy conversion and sustainability.

Data availability

Crystallographic data for the compounds have been deposited at the Cambridge Crystallographic Data Centre (CCDC) with the accession numbers 2395420, 2373983–2373985, which can be accessed at **https://www.ccdc.cam.ac.uk/**. Materials and methods, detailed synthesis and additional characterization of the synthesized samples, photocatalytic tests, and DFT calculations are provided in the ESI† accompanying this article. This information is accessible at **https://doi.org/10.1039/D5SC02797G**.

Author contributions

Yi-Fan Liu and Huihui He contributed equally to this work. Yi-Fan Liu: conceptualization, investigation, formal analysis, visualization, writing – original draft, methodology; Huihui He: formal analysis, investigation, visualization, validation, methodology, writing – original draft; Lei Gao: formal analysis, software; Rong-Ran Liang: data curation, formal analysis; Ji Li: investigation, resources; Jinyi Huang: investigation, resources; Ya Yin: investigation; Yuxuan Meng: investigation; Yuxiu Zhong: investigation; Rengan Luo: investigation, funding acquisition; Liang–Liang Zhang: conceptualization, writing – review & editing, funding acquisition; Hong-Cai Zhou: conceptualization, writing – review & editing, supervision; Shuai Yuan: conceptualization, writing – review & editing, project administration, supervision, funding acquisition.

Conflicts of interest

There are no conflicts to declare.

Acknowledgements

This work was financially supported by the National Key Research and Development Program of China (2024YFA1510301), the National Natural Science Foundation of China (No. 22271141), Natural Science Foundation of Fujian Province (Grant No. 2023J01294), Fundamental Research Funds for the Central Universities (2024300376), the Postdoctoral Fellowship Program of CPSF (GZB20240303), the China Postdoctoral Science Foundation (2024M751374), and the Jiangsu Funding Program for Excellent Postdoctoral Talent (2024ZB547). We thank the staff of the BL17B beamline (**https://cstr.cn/31129.02.NFPS.BL17B**) at the National Facility for Protein Science in Shanghai (NFPS, **https://cstr.cn/31129.02.NFPS**), Shanghai Advanced Research Institute, Chinese Academy of Sciences, for their technical support in Single-crystal XRD data collection and analysis. The numerical calculations in this paper have been done using the computing facilities of the High Performance Computing Center (HPCC) at Nanjing University.

Notes and references

1 P. N. Trikalitis, K. K. Rangan, T. Bakas and M. G. Kanatzidis, *Nature*, 2001, **410**, 671–675.
2 J. Kou, C. Lu, J. Wang, Y. Chen, Z. Xu and R. S. Varma, *Chem. Rev.*, 2017, **117**, 1445–1514.
3 S. Zhu and D. Wang, *Adv. Energy Mater.*, 2017, **7**, 1700841.
4 Q. Guo, C. Zhou, Z. Ma and X. Yang, *Adv. Mater.*, 2019, **31**, 1901997.
5 D. Li, M. Kassymova, X. Cai, S.-Q. Zang and H.-L. Jiang, *Coord. Chem. Rev.*, 2020, **412**, 213262.
6 L. Jiang, J. Yang, S. Zhou, H. Yu, J. Liang, W. Chu, H. Li, H. Wang, Z. Wu and X. Yuan, *Coord. Chem. Rev.*, 2021, **439**, 213947.
7 T. M. R. Asahi, T. Ohwaki, K. Aoki and Y. Taga, *Science*, 2001, 269–271.
8 R. Zhou, B. Qu, D. Li, X. Sun and X. C. Zeng, *Adv. Funct. Mater.*, 2018, **28**, 1705529.
9 I. Shown, S. Samireddi, Y.-C. Chang, R. Putikam, P.-H. Chang, A. Sabbah, F.-Y. Fu, W.-F. Chen, C.-I. Wu, T.-Y. Yu, P.-W. Chung, M. C. Lin, L.-C. Chen and K.-H. Chen, *Nat. Commun.*, 2018, **9**, 169.
10 T. Takata, J. Jiang, Y. Sakata, M. Nakabayashi, N. Shibata, V. Nandal, K. Seki, T. Hisatomi and K. Domen, *Nature*, 2020, **581**, 411–414.
11 Y. Zhang, Y. Li, X. Xin, Y. Wang, P. Guo, R. Wang, B. Wang, W. Huang, A. J. Sobrido and X. Li, *Nat. Energy*, 2023, **8**, 504–514.
12 H. B. Gray, *Nat. Chem.*, 2009, **1**, 7.
13 J. Liu, Y. Liu, N. Liu, Y. Han, X. Zhang, H. Huang, Y. Lifshitz, S.-T. Lee, J. Zhong and Z. Kang, *Science*, 2015, **347**, 970–974.
14 J. Wang, Y. Shi, Y. Wang and Z. Li, *ACS Energy Lett.*, 2022, **7**, 2043–2059.
15 H. Yang, K. Dai, J. Zhang and G. Dawson, *Chinese J. Catal.*, 2022, **43**, 2111–2140.
16 Z.-Y. Chen, N.-Y. Huang and Q. Xu, *Coord. Chem. Rev.*, 2023, **481**, 215031.
17 M. E. Hailian Li, M. O'Keeffe and O. M. Yaghi, *Nature*, 1999, **402**, 276–279.
18 H. C. Zhou, J. R. Long and O. M. Yaghi, *Chem. Rev.*, 2012, **112**, 673–674.
19 A. Helal, Z. H. Yamani, K. E. Cordova and O. M. Yaghi, *Natl. Sci. Rev.*, 2017, **4**, 296–298.
20 J.-L. Wang, C. Wang and W. Lin, *ACS Catal.*, 2012, **2**, 2630–2640.
21 A. Dhakshinamoorthy, Z. Li and H. Garcia, *Chem. Soc. Rev.*, 2018, **47**, 8134–8172.
22 N. Li, J. Liu, J.-J. Liu, L.-Z. Dong, Z.-F. Xin, Y.-L. Teng and Y.-Q. Lan, *Angew. Chem., Int. Ed.*, 2019, **58**, 5226–5231.
23 T. Luo, L. Gilmanova and S. Kaskel, *Coord. Chem. Rev.*, 2023, **490**, 215210.

24 A. Dhakshinamoorthy, Z. Li, S. Yang and H. Garcia, *Chem. Soc. Rev.*, 2024, **53**, 3002–3035.
25 Y. H. Kiang, G. B. Gardner, S. Lee, Z. Xu and E. B. Lobkovsky, *J. Am. Chem. Soc.*, 1999, **121**, 8204–8215.
26 J. S. Seo, D. Whang, H. Lee, S. I. Jun, J. Oh, Y. J. Jeon and K. Kim, *Nature*, 2000, **404**, 982–986.
27 Z. Wang and S. M. Cohen, *Chem. Soc. Rev.*, 2009, **38**, 1315–1329.
28 H. Fei, M. D. Sampson, Y. Lee, C. P. Kubiak and S. M. Cohen, *Inorg. Chem.*, 2015, **54**, 6821–6828.
29 T. Kajiwara, M. Fujii, M. Tsujimoto, K. Kobayashi, M. Higuchi, K. Tanaka and S. Kitagawa, *Angew. Chem., Int. Ed.*, 2016, **55**, 2697–2700.
30 Y. Chen, P. Li, J. Zhou, C. T. Buru, L. Đorđević, P. Li, X. Zhang, M. M. Cetin, J. F. Stoddart, S. I. Stupp, M. R. Wasielewski and O. K. Farha, *J. Am. Chem. Soc.*, 2020, **142**, 1768–1773.
31 J. Li, H. Huang, W. Xue, K. Sun, X. Song, C. Wu, L. Nie, Y. Li, C. Liu, Y. Pan, H.-L. Jiang, D. Mei and C. Zhong, *Nat. Catal.*, 2021, **4**, 719–729.
32 X. Feng, Y. Pi, Y. Song, C. Brzezinski, Z. Xu, Z. Li and W. Lin, *J. Am. Chem. Soc.*, 2020, **142**, 690–695.
33 P. M. Stanley, A. Y. Su, V. Ramm, P. Fink, C. Kimna, O. Lieleg, M. Elsner, J. A. Lercher, B. Rieger, J. Warnan and R. A. Fischer, *Adv. Mater.*, 2023, **35**, 2207380.
34 Z. Zhang, D. Deng, X. Xu, J. Zhang, S. Yan, Z. Guo, H. Dong, Z. Chen and Z. Su, *JACS Au*, 2024, **4**, 2050–2057.
35 S. Yuan, W. Lu, Y.-P. Chen, Q. Zhang, T.-F. Liu, D. Feng, X. Wang, J. Qin and H.-C. Zhou, *J. Am. Chem. Soc.*, 2015, **137**, 3177–3180.
36 S. Yuan, Y.-P. Chen, J.-S. Qin, W. Lu, L. Zou, Q. Zhang, X. Wang, X. Sun and H.-C. Zhou, *J. Am. Chem. Soc.*, 2016, **138**, 8912–8919.
37 C.-X. Chen, Z.-W. Wei, J.-J. Jiang, S.-P. Zheng, H.-P. Wang, Q.-F. Qiu, C.-C. Cao, D. Fenske and C.-Y. Su, *J. Am. Chem. Soc.*, 2017, **139**, 6034–6037.
38 X.-J. Hu, Z.-X. Li, H. Xue, X. Huang, R. Cao and T.-F. Liu, *CCS Chem.*, 2020, **2**, 616–622.
39 Q. Zhang, J. Su, D. Feng, Z. Wei, X. Zou and H.-C. Zhou, *J. Am. Chem. Soc.*, 2015, **137**, 10064–10067.
40 J.-S. Qin, S. Yuan, L. Zhang, B. Li, D.-Y. Du, N. Huang, W. Guan, H. F. Drake, J. Pang, Y.-Q. Lan, A. Alsalme and H.-C. Zhou, *J. Am. Chem. Soc.*, 2019, **141**, 2054–2060.
41 P. Dong, X. Xu, R. Luo, S. Yuan, J. Zhou and J. Lei, *J. Am. Chem. Soc.*, 2023, **145**, 15473–15481.
42 Z. Wei, Z.-Y. Gu, R. K. Arvapally, Y.-P. Chen, R. N. McDougald, Jr., J. F. Ivy, A. A. Yakovenko, D. Feng, M. A. Omary and H.-C. Zhou, *J. Am. Chem. Soc.*, 2014, **136**, 8269–8276.
43 P. Giannozzi, S. Baroni, N. Bonini, M. Calandra, R. Car, C. Cavazzoni, D. Ceresoli, G. L. Chiarotti, M. Cococcioni, I. Dabo, A. Dal Corso, S. de Gironcoli, S. Fabris, G. Fratesi, R. Gebauer, U. Gerstmann, C. Gougoussis, A. Kokalj, M. Lazzeri, L. Martin-Samos, N. Marzari, F. Mauri, R. Mazzarello, S. Paolini, A. Pasquarello, L. Paulatto, C. Sbraccia, S. Scandolo, G. Sclauzero, A. P. Seitsonen, A. Smogunov, P. Umari and R. M. Wentzcovitch, *J. Phys.: Condens. Matter*, 2009, **21**, 395502.
44 P. Giannozzi, O. Baseggio, P. Bonfà, D. Brunato, R. Car, I. Carnimeo, C. Cavazzoni, S. de Gironcoli, P. Delugas, F. Ferrari Ruffino, A. Ferretti, N. Marzari, I. Timrov, A. Urru and S. Baroni, *J. Chem. Phys.*, 2020, **152**, 154105.
45 A. M. Rappe, K. M. Rabe, E. Kaxiras and J. D. Joannopoulos, *Phys. Rev. B*, 1990, **41**, 1227–1230.
46 S. M. Pratik, L. Gagliardi and C. J. Cramer, *Chem. Mater.*, 2020, **32**, 6137–6149.
47 J. Yu, J. Park, A. Van Wyk, G. Rumbles and P. Deria, *J. Am. Chem. Soc.*, 2018, **140**, 10488–10496.
48 N. C. Chiu, J. M. Lessard, E. N. Musa, L. S. Lancaster, C. Wheeler, T. D. Krueger, C. Chen, T. C. Gallagher, M. T. Nord, H. Huang, P. H.-Y. Cheong, C. Fang and K. C. Stylianou, *Nat. Commun.*, 2024, **15**, 1459.
49 W. Hu, D. Wang, Q. Ma, B. J. Reinhart, X. Zhang and J. Huang, *J. Photochem. Photobiol., A*, 2022, **11**, 100132.